Insights into the alloy-support synergistic effects for the CO_2 hydrogenation towards methanol on oxide-supported Ni_5Ga_3 catalysts: An experimental and DFT study

Letícia F. Rasteiro [a], Rafael A. De Sousa [a], Luiz H. Vieira [a,b], Vivianne K. Ocampo-Restrepo [a], Lucas G. Verga [a], José M. Assaf [b], Juarez L.F. Da Silva [a], Elisabete M. Assaf [a,*]

[a] *University of São Paulo, São Carlos Institute of Chemistry, Av. Trabalhador São-Carlense, 400, 13560-970 São Carlos, SP, Brazil*
[b] *Federal University of São Carlos, Chemical Engineering Department, Rod. W. Luiz, km 235, 13565-905 São Carlos, SP, Brazil*
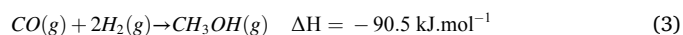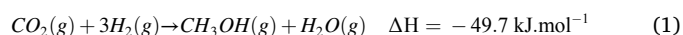
ARTICLE INFO

ABSTRACT

Supported Ni-Ga alloys have emerged as potential catalyst to mitigate CO_2 emissions by its conversion into methanol at mild conditions, however, its performance depends on the optimization of the alloy-support effects, which is unclear up to now. Herein, we investigate the influence of alloy-support synergy in the catalytic performance of Ni_5Ga_3 supported on SiO_2, CeO_2, and ZrO_2, by combining in-depth structural, chemical and spectroscopic characterization and density functional theory (DFT) calculations. *In situ* DRIFTS confirmed further hydrogenation of key reaction intermediates in Ni_5Ga_3/ZrO_2 surface, while weak CO_2 adsorption in Ni_5Ga_3/SiO_2 avoided intermediate stabilization on the surface and, strong interaction with Ni_5Ga_3/CeO_2 poisoned interface active sites. Additionally, the relative energies of reactants and key intermediates in the three distinct regions of the catalyst (support surface, alloy surface, and alloy-support interface), calculated through DFT, allowed us to propose a reaction mechanism for the most promising catalyst, Ni_5Ga_3/ZrO_2.

1. Introduction

Carbon capture and utilization (CCU) is a promising way to alleviate the high levels of CO_2 in the atmosphere and bring economic gain at the same time [1,2]. Among several options for CO_2 utilization, the hydrogenation to methanol has gained great attention worldwide due to the promising methanol economy [3]. Methanol is an important C1 building block used to produce valuable chemicals like acetic acid, dimethyl ether, olefins, among others [4]. The CO_2 molecule is extremely stable, and the hydrogenation to produce methanol is an exothermic reaction (Eq. (1)) favored at lower temperatures [5]. Another route that is involved in methanol synthesis through CO_2 hydrogenation is the reverse water-gas shift (rWGS) (Eq. (2)), which is an endothermic reaction, favored as temperature increases. If the CO produced by rWGS continues to be hydrogenated, methanol can also be formed (Eq. (3)) [5].

$$CO_2(g) + 3H_2(g) \rightarrow CH_3OH(g) + H_2O(g) \quad \Delta H = -49.7 \text{ kJ.mol}^{-1} \quad (1)$$

$$CO_2(g) + H_2(g) \leftrightharpoons CO(g) + H_2O(g) \quad \Delta H = +41.2 \text{ kJ.mol}^{-1} \quad (2)$$

$$CO(g) + 2H_2(g) \rightarrow CH_3OH(g) \quad \Delta H = -90.5 \text{ kJ.mol}^{-1} \quad (3)$$

Cu/ZnO-based catalysts have been extensively studied for methanol production through CO_2 hydrogenation. However, these types of catalysts need high pressure to achieve good selectivity to methanol, and they deactivate over the reaction time [1,6]. These catalysts are based on $CuZnO/Al_2O_3$ industrial catalyst for CO hydrogenation, carried out in the pressure range of 50–100 bar [7]. In a study about thermo-economic

aspects of a CO_2 hydrogenation plant, Bellotti et al. [8] show that the energy waste to compress $CO_2 + H_2$ gases to 80 bar is 57% higher than the energy waste to operate the same gases at 30 bar. So, search for catalysts that are more selective to methanol at low pressures can be more economically feasible for industrial plants. Therefore, noncopper-based catalysts started to be studied as alternatives and are gaining more attention in the last years, like Pd-based catalysts [9,10], metal-organic-framework (MOF) catalysts [11–13], and bimetallic catalysts (Pd-Ga [14], Pd-Cu [15], and Ni-Ga [16]), that presented good activity for methanol production.

Recently, a theoretical/experimental study by Studt et al. [16] reported Ni_5Ga_3/SiO_2 as an active catalyst at ambient pressure with similar methanol selectivity and lower CO selectivity than the industrial $CuZnO/Al_2O_3$ catalyst in CO_2 hydrogenation to methanol. From this, the study of Ni-Ga alloys as catalysts to CO_2 hydrogenation to methanol started to gain attention in the scientific community [4,17–22]. The subsequent studies applying Ni-Ga-based catalysts have found interesting improvements on methanol production during the reaction by focusing on parameters like catalyst preparation and activation, the effect of promoters, and the role of Ni_5Ga_3 crystalline structure in the activity. The thermal treatments during preparation and activation of catalysts were found to strongly affect the performance during CO_2 hydrogenation. The direct reduction of gallium and nickel precursors, with no previous calcination, on Ni-Ga/SiO_2 catalysts was reported to result in the formation of smaller alloy nanoparticles benefiting methanol selectivity [19]. Additionally, it was found that the previous *ex-situ* reduction of the catalyst at higher temperatures (700 °C) followed by exposure to air, can favor the migration of gallium from the subsurface region to the surface forming a Ga_2O_3 shell in Ni-Ga nanoparticles, which after a low-temperature re-activation (400 °C) increased the methanol productivity from 26.4 to 32.3 μmol_{CH3OH} m^{-2} h^{-1} and considerably decreased CO uptake from 83.2 to 26.5 μmol g_{cat}^{-1} when compared to conventional high-temperature *in-situ* activation [22]. The effect of promoters on the Ni-Ga alloy structure was also investigated. The presence of Fe in the Ni-Ga catalyst under optimized composition and reduction conditions (Ni_2FeGa, 550 °C) resulted in the formation of fully ternary metallic nanoparticles and prevented sintering, achieving catalytic performance comparable to the commercial copper-based methanol synthesis catalyst, $CuZnO/Al_2O_3$, above 200 °C but low selectivity at higher temperatures [21]. The addition of other metals like Cu, Co, and Au as promoters allowed to identify the influence of a third metal in the formation of Ni-Ga intermetallic phase and in the number of available sites for CO chemisorption, in which weak CO adsorptions were more beneficial to methanol production than stronger ones [23]. The catalyst structure also plays an important role in catalytic activity. The preparation of a Ni_5Ga_3 catalyst from hydrotalcite-like precursor at different temperatures was explored in a recent study and it was observed that the catalyst synthesized at 110 °C produced smaller crystal sizes, stable structure, and higher activity for CO_2 hydrogenation to methanol [4]. Despite the growing interest in Ni-Ga catalysts, little has been explored regarding Ni-Ga fundamentals characteristics and mechanisms in the catalytic reaction. Our previous study [18] was the only one, to the best of our knowledge, that experimentally proposed a mechanism for CO_2 hydrogenation to methanol over an unsupported Ni_5Ga_3 alloy.

The use of ZrO_2 and CeO_2 as supports for Cu catalysts applied on CO_2 hydrogenation has shown great catalytic performance in terms of methanol production [24–27]. The structural and adsorption properties of metal-support interaction along with the redox properties seem to be extremely beneficial and lead to better catalytic activity [24]. However, these supports, to the best of our knowledge, were never investigated in Ni-Ga systems. The only Ni-Ga works that studied the effect of support different from SiO_2 were of Chen et al. [17], which studied the use of a $SiO_2/Al_2O_3/Al$-fiber support, and Goyal et al. [20], that studied Ni-Ga dispersed on nitrogen-doped mesoporous carbon materials and both studies focused on the effect of different compositions of the supports on methanol production.

Hence, in this paper, we evaluate the role of the alloy-support interface in the optimization of methanol production during CO_2 hydrogenation by preparing Ni_5Ga_3 catalysts on the CeO_2, ZrO_2 and SiO_2 supports. Catalytic performance and structural, chemical, and surface properties were correlated by applying several characterization techniques, revealing the additional effect of interface synergy in Ni_5Ga_3/ZrO_2 as a promoter for methanol productivity. Additionally, *in situ* diffuse reflectance infrared Fourier transform spectroscopy (DRIFTS) and density functional theory (DFT) calculations were performed to obtain insights into the role of the alloy-support interface in the stabilization of key reaction intermediates and to discuss its effects on the reaction mechanism for the promising catalyst.

2. Methods

2.1. Catalyst preparation

The synthesis of the CeO_2 and ZrO_2 supports was carried out in the same way, differing only in the masses of the $ZrO(NO_3)_2 \cdot 5H_2O$ and $Ce(NO_3)_3 \cdot 6H_2O$ salts, being 7.433 and 7.569 g, respectively. The mass of the respective salt was weighed, diluted in 40 mL of distilled water, and left under stirring until complete dissolution. Then 12 mL of NH_4OH (14.7 M) was dripped and left under stirring for another 30 min. After that, the solution was filtered and the solid was re-dispersed in 100 mL of NH_4OH (0.25 M). Finally, the solid was dried at 70 °C for 24 h and calcined at 500 °C for 4 h, resulting in the supports CeO_2 and ZrO_2. The synthesis of the supported alloys was carried out through the wet impregnation of the $Ni(NO_3)_2$ and $Ga(NO_3)_3$ salts. The Ni/Ga molar ratio used was 5/3 and it was impregnated 17% by weight of the Ni + Ga metals on CeO_2, ZrO_2 and commercial SiO_2 supports. The resulting catalysts were calcined at 500 °C for 2 h and named NGCe, NGZr, and NGSi.

2.2. Catalyst characterization

Structural properties of catalysts were investigated by combining X-ray diffraction (XRD), gas physisorption isotherms (N_2-sorption), and transmission electron microscopy (TEM) techniques. XRD was performed to analyze the crystalline phases formed in the catalysts. A BRUKER APEX II Duo diffractometer was used, operating with Cu Kα radiation (0.15418 nm), selected with a curved graphite monochromator. The data were collected with a scan speed of 0.02° s^{-1} over the 2θ range of 5–100°. Crystallographica Search Match software was used to identify the crystalline phases of the samples and TOPAS® 5 software was used to quantify ZrO_2 crystalline phases by the Rietveld refinement method. Nitrogen sorption measurements were performed to determine the specific surface area (S_{BET}) by Brunauer-Emmett-Teller model (BET) and pore diameter distribution by the Barret-Joyner-Halenda model (BJH). The experiments were performed using a Quantachrome Nova 1000e system at liquid nitrogen temperature (-196 °C), with relative pressure intervals between 0.001 and 0.998. The pretreatment of the samples was made under vacuum ($\sim 10 \times 10^{-6}$ Pa) for 4 h at 200 °C. Transmission electron microscopy (TEM) analyses were made using a JEOL JEM2100 LaB6 instrument operated at 200 kV. The samples were prepared for the measurement being dispersed in isopropanol by ultrasonication, dropping the suspension in Cu grids, and then dried for 48 h. The particle size distribution was obtained by counting around 100 particles for each catalyst from TEM images.

The chemical composition and surface properties of catalysts were investigated by combining energy dispersive X-ray fluorescence spectroscopy (ED-XRF), temperature programmed analysis, and X-ray photoelectron spectroscopy (XPS). ED-XRF was performed to estimate the elementary composition of catalysts by using a MiniPal 4 PANalytical spectrometer. Temperature programmed reduction (TPR) analysis was conducted on a Micromeritics Pulse ChemSorb 2750 instrument

equipped with a thermal conductivity detector (TCD). 100 mg of catalyst was inserted into the reactor and the whole system was heated from room temperature to 900 °C, at the rate of 10 °C min^{-1}, using a 10% H$_2$/Ar gaseous mixture at a flow rate of 30 mL min^{-1} as reductant. A U-tube trap cooled to 0 °C was placed between reactor and detector to avoid H$_2$O formed during the reduction process to reach the detector. Temperature programmed desorption of CO$_2$ (CO$_2$-TPD) was performed to quantify the basic sites present in the catalysts from room temperature to 500 °C. First, the samples were reduced to 500 °C for 1 h under a 10% H$_2$/He atmosphere, then they were cooled to room temperature under He flow (20 mL/min) and then cleaned with Ar for 30 min. After this step, the catalysts were heated to 40 °C and saturated with CO$_2$ (20 mL/min) for 30 min. Then, the system was cooled to room temperature and a flow of 20 mL/min of Ar was left for 1 h to remove physisorbed CO$_2$ from the catalyst surface. The experiment was carried out with heating at 5 °C/min under Ar flow (20 mL/min) up to 500 °C. Temperature-programmed desorption of H$_2$ (TPD-H$_2$) measurements was carried out using a Micromeritics Pulse ChemSorb 2750 instrument equipped with a thermal conductivity detector (TCD). First, the catalyst was reduced at 500 °C for 1 h and then the temperature was decreased to 25 °C. The gaseous mixture (10% H$_2$/Ar) was passed over the catalysts at the flow rate of 30 mL min^{-1} for 60 min. The physisorbed gas was removed by purging with argon for 30 min. The temperature was raised to 900 °C at 5 °C min^{-1} under argon flow and the data was collected during the heating. XPS analysis was carried on a Kratos AXIS ULTRADLD XPS spectrometer equipped with an Al Kα monochromatic X-ray source and a 165-mm mean radius electron energy hemispherical analyzer with a slot. During the data acquisition, the vacuum pressure was kept below 3×10^{-9} torr and a neutralizer was applied to compensate sample charging during the measurement. The inelastic background of the spectra was subtracted using Shirley's equation. The binding energy scale of the spectra was corrected using the C1s hydrocarbon group at 284.8 eV. The spectra were deconvolved using a Voigtian function with the combination of Lorentzian (30%) and Gaussian (70%) functions.

To investigate the formation and evolution of surface species during the reaction, *in situ* Fourier-transform infrared spectroscopy in a Shimadzu IRPrestige-21 FTIR instrument equipped with a diffuse reflectance (DRIFT) accessory and a Harrick cell with ZnSe windows. For monitoring the CO$_2$ hydrogenation reaction, the catalyst was pre-treated at 550 °C in H$_2$ flow (30 mL min^{-1}) for 1 h and cooled to 270 °C to collect the background. The reaction was monitored for 30 min at 270 °C by flowing 30 mL min^{-1} of a mixture containing 25% CO$_2$/75% H$_2$ through the cell. Additionally, experiments with separate steps of CO$_2$ adsorption, surface purge with N$_2$, and H$_2$ flow were carried in supports and catalysts and monitored by DRIFTS. The spectra were obtained at a resolution of 4 cm^{-1} by averaging 64 sequentially collected scans.

2.3. Catalytic activity

The catalytic activity for CO$_2$ hydrogenation over Ni-Ga catalysts was evaluated in a stainless-steel fixed-bed tubular reactor (304.3 mm length, 9.1 mm internal diameter). Typically, 150 mg of the catalyst was used, packed with quartz wool. Before each test, the catalyst was *in situ* reduced at 500 °C for 1 h, in 30 mL min^{-1} of pure H$_2$ at atmospheric pressure, to achieve the complete insertion of gallium atoms in the alloy structure generating a Ni$_5$Ga$_3$-phase exposed surface, as previously reported [19]. After the reduction, the reactor was cooled to a specific temperature (180, 225, or 270 °C) and the gas flow was switched to the desired flow rate of H$_2$/CO$_2$ (8000; 24,000; or 40,000 L kg$_{cat}$$^{-1}$ h^{-1}) at a molar ratio of 3:1. The system was also pressurized to the desired pressure before starting the reaction. The reaction time for each condition was 2 h to ensure stable conversion and the pressure was varied from ambient pressure to 30 bar. With the aim of comparison, CuZnO/Al$_2$O$_3$ (CZA) was tested in the CO$_2$ hydrogenation to methanol at

270 °C, 8000 L kg$_{cat}$$^{-1}$ h^{-1}, at 30 bar and ambient pressure. The gases produced were analyzed by an online gas chromatograph (Agilent Technologies 7890A) equipped with a flame ionization detector (FID) for the analysis of methanol and methane, and a thermal conductivity detector (TCD) for the analysis of CO, H$_2$, and CO$_2$. The analysis was made every 15 min. The CO$_2$ conversion and product selectivity (CO, CH$_3$OH, and CH$_4$), were calculated as follows:

$$\text{Selectivity to } i(\%) = \left(\frac{f_i A_{i,out}}{\sum f_i A_{i,out}} \right) \times 100 \qquad (4)$$

$$CO_2 \, conversion \quad (\%) = \left(\frac{CO_{2,in} - CO_{2,out}}{CO_{2,in}} \right) \times 100 \qquad (5)$$

where, $A_{i,out}$ and f_i represent the chromatogram peak area and the molar calibration factor, respectively, for each chemical species i (i = CH$_3$OH, CH$_4$, and CO) at the output. The two terms, $CO_{2,in}$ and $CO_{2,out}$, represent the total number of mols of CO$_2$ that enter and exit the reactor, respectively, which are required to measure the CO$_2$ conversion. The space-time yield of methanol (g$_{MeOH}$ kg$_{cat}$$^{-1}$ h^{-1}) was calculated by the following equation:

$$STY(\textit{Space Time Yield}) = \frac{X_{CO2} \times S_{CH3OH} \times F_{CO2,in} \times MW_{CH3OH}}{W_{cat} \times V_m} \qquad (6)$$

where X_{CO2} is the conversion of CO$_2$, S_{CH3OH} is the selectivity to CH$_3$OH, $F_{CO2,in}$ is the volumetric flow rate of CO$_2$ (mL h^{-1}), MW_{CH3OH} is the molecular weight of methanol (32 g mol^{-1}), W_{cat} is the catalyst weight used (kg), and V_m is the ideal gas molar volume at standard pressure and temperature (mL mol^{-1}).

To determine the turnover frequency (TOF) of the catalysts, the alloy surface was established as the active sites and the metallic area (Eq. (S1)) was applied in the TOF calculations. The turnover frequency (TOF) of methanol was calculated by the following equations [28]:

$$TOF_{CH3OH}\left(s^{-1}\right) = \frac{Number \ of \ molecules \ of \ methanol \ produced}{Time \ (s) \ \times \ Number \ of \ metallic \ Ni_5Ga_3 \ atoms} \qquad (7)$$

$$TOF_{CH3OH}\left(s^{-1}\right) = \frac{A \times \mathscr{N}a}{3600 \ \times \ S_{Ni5Ga3} \ \times \ Na} \qquad (8)$$

where A represents methanol activity in mol g^{-1} h^{-1}, $\mathscr{N}a$ is Avogadro's number (6.023×10^{23} atoms mol^{-1}), S_{Ni5Ga3} denotes Ni$_5$Ga$_3$ surface area in m^2 g^{-1} and Na designates the number of Ni$_5$Ga$_3$ atoms in a monolayer ($Na = 1.58 \times 10^{19}$ atoms m^{-2}). The number of atoms was estimated considering a monolayer in the [001] plane of an orthorhombic (*Cmmm*) Ni$_5$Ga$_3$ unit cell.

2.4. Theoretical approach and computational details

Total energy calculations were performed with the spin-polarized framework and employing the Perdew-Burke-Erzenhorf [29] exchange-correlation functional. The Tkatchenko-Scheffler [30] (TS) method was employed to describe more accurately long-range Van der Waals (VdW) interactions. The Kohn-Sham equations were solved with the all-electron full-potential Fritz-Haber Institute *ab initio* molecular simulations (FHI-aims) package [31]. Minimal basis set for free-atom orbitals together with an additional set of functions added up to the second basis set improvement, called light-tier2 in FHI-aims notation, were used as basis set. The models to study the interaction of CO$_2$ intermediates were based on a (ZrO$_2$)$_{16}$ cluster that was obtained from a publication by Puigdollers et al. [32], while Ni$_5$Ga$_3$ and Ni$_5$Ga$_3$/(ZrO$_2$)$_{16}$ systems were obtained following a set of computational procedures. Specifically, Ni$_5$Ga$_3$ structures were obtained by replacing Ni atoms with Ga atoms on several Ni$_8$ structures and applying a K-means Clustering Algorithm [33] to select 50 structures to be optimized. The selected

$(ZrO_2)_{16}$ and Ni_5Ga_3 structures were later used together with an in-house Euclidian Similarity Distance (ESD) algorithm [34,35] to generate supported $Ni_5Ga_3/(ZrO_2)_{16}$ systems and adsorbate configurations on Ni_5Ga_3, $(ZrO_2)_{16}$, and $Ni_5Ga_3/(ZrO_2)_{16}$ (NGZr) systems. More details of the procedures and employed algorithms can be found within the Supplementary information, Section 1-SI.

3. Results and discussion

### 3.1. Impact of support nature on the activity in CO_2 hydrogenation to methanol

Fig. 1A–C show the results of the catalytic reactions at different temperatures, space velocities (GHSV), and pressures for the NGSi, NGZr, and NGCe catalysts. The other products formed in addition to methanol were methane and carbon monoxide (Fig. S1). Initially, the effect of temperature was verified (Fig. 1A) with the pressure maintained in 10 bar at a GHSV of 8000 L kg_{cat}^{-1} h^{-1}. For all the systems, the conversions increased by raising the temperature, and the highest values occurred for NGCe catalyst, followed by NGZr and finally NGSi. Despite the good catalytic activity, NGCe showed poor methanol selectivity, with most of CO_2 converting into CO, at around 90% of selectivity.

Analyzing the methanol selectivity, it is noted that it decreases with the increase of the reaction temperature for both NGCe and NGSi catalysts. Interestingly, this effect was not observed for the NGZr catalyst, which undergoes a small increase in selectivity when the temperature increased from 180 to 225 °C and remains constant by increasing to 270 °C. At 180 and 225 °C, the NGSi catalyst presented the highest methanol selectivity. At 270 °C, the NGZr catalyst starts to present the best selectivity among the catalysts. The NGCe catalyst has the lowest selectivity for methanol at all temperatures studied. The CO selectivity (Fig. S1) presented different behavior between the catalysts, whereupon for NGSi CO selectivity increased with the temperature increase as expected since at higher temperatures the rWGS is favored due to its endothermic character. For NGZr and NGCe, the CO selectivity presented a small decrease ranging from 10% to 5%. This behavior is related to the different interaction strengths of the intermediates with the catalysts, which are investigated in the following sections. Observing methanol productivity (Fig. 1D), it is noted that the catalysts supported on CeO_2 and ZrO_2 had the highest values and among them, the NGZr catalyst had the highest methanol production, with a significant increase at 270 °C.

Maintaining the temperature at 270 °C and the pressure at 10 bar, the effect of GHSV in the activity was verified for the catalysts (Fig. 1B). Note that the selectivity remained constant for all catalysts, but there was a drop in conversion with the increase in GHSV. This drop in the conversion can be explained due to the shorter contact time that CO_2 and H_2 molecules had with the catalyst when the flow of gases increased, which consequently should lead to a decrease in conversion. Thus, the increase in gas flow was not advantageous for our catalytic system, which we also observed in our previous work with the unsupported Ni-Ga alloys [18]. By keeping the temperature at 270 °C and the GHSV at 8000 L $kg_{cat}^{-1}.h^{-1}$, the effect of pressure was verified for the catalytic system applying NGZr as catalyst (Fig. 1C), which previously presented the best methanol productivity (160.1 g_{CH3OH} kg_{cat}^{-1} h^{-1}). The increase from ambient pressure to 10 bar led to a remarkable increase in conversion, remaining approximately constant in the subsequent increases to 20 and 30 bar. In terms of selectivity, however, the increase was more consistent and, consequently, in methanol productivity as well, reaching 272.5 g_{CH3OH} kg_{cat}^{-1} h^{-1} at 30 bar, which is explained by the Le Châtelier principle, considering the stoichiometry of the reaction. In addition, the catalyst proved to be active at ambient pressure, which is a highly desired property for the chemical industry. The *turnover frequency* (TOF) data for catalysts in the optimized catalytic conditions (Table S1), revealed values of 0.35, 0.72, and 1.34 ($\times 10^{-3}$ s^{-1}) for NGSi, NGCe, and NGZr, respectively. As the TOF allows the determination of the intrinsic activity of the catalytic site [36], the results clearly indicate a superior efficiency of catalytic sites in NGZr catalyst.

Most of reports regarding NiGa systems for CO_2 hydrogenation to methanol are based in the use of unsupported or SiO_2-supported catalysts, as observed in Table S2. The previous results clearly indicate that the superior alloy dispersion promoted by using supports are essential to increase catalytic activity when compared to unsupported ones. Although the promoting effects of physical dispersion of the active
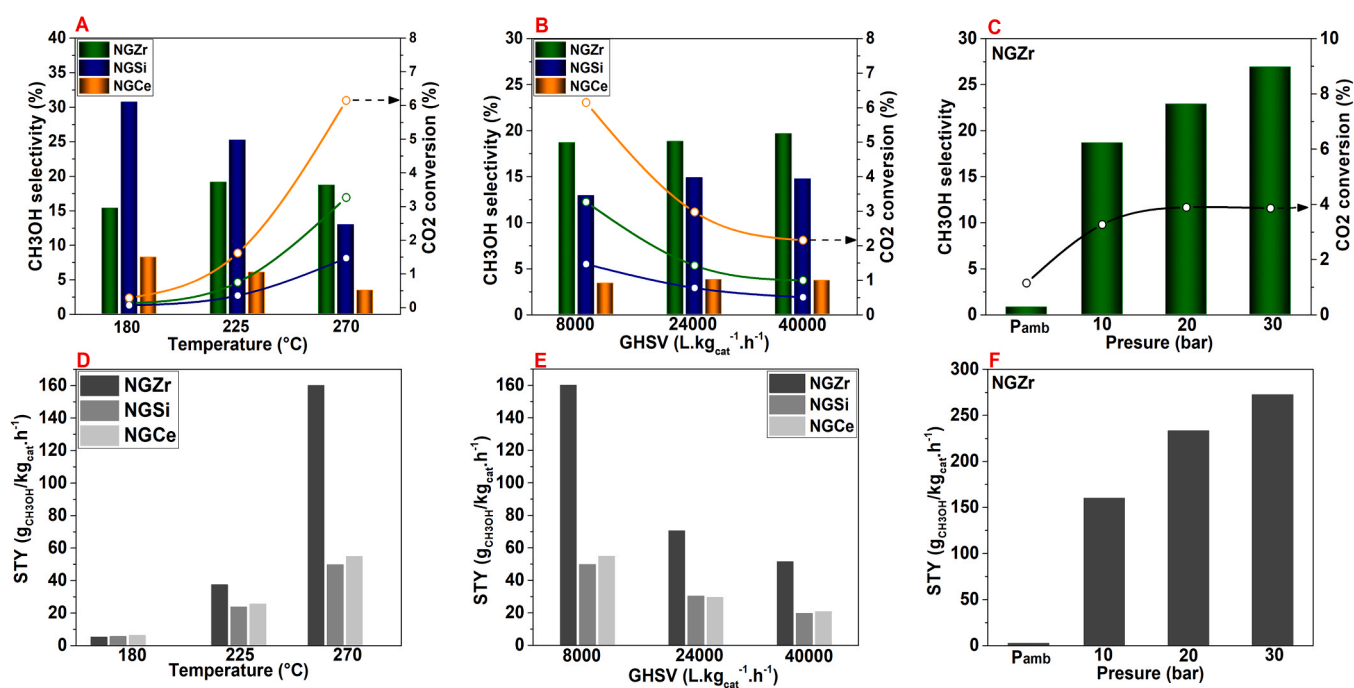
Fig. 1. Catalytic tests with selectivity for methanol and conversion for catalysts varying (A) temperature, (B) GHSV, and (C) pressure. Productivities in g_{CH3OH} kg_{cat} h^{-1} for methanol varying (D) temperature, (E) GHSV and (F) pressure.

phase, comparing these results with our catalysts, we can note that the chemical nature of oxide support, especially for materials that present distinct interactions with CO_2, has an important role and considerably affect the activity to methanol production. The NGZr catalyst of this work showed improved methanol productivity, when compared to unsupported and SiO_2-supported catalysts reported, probably associated with the generated alloy-support interface phenomena, which will be investigated below. Besides, Ni_5Ga_3/ZrO_2 catalytic performance, it can still be optimized in further studies considering reaction parameters and catalyst design.

The selectivity results for methanol and CO by applying the NGZr catalyst and $CuZnO/Al_2O_3$ (CZA), the currently industrial catalyst applied for the hydrogenation of CO, in the same conditions were compared in Table 1. The NGZr presented selectivity for methanol at ambient pressure (AP) of approximately ten times higher than the CZA catalyst, in addition to also having a lower selectivity for CO. The same behavior occurs for selectivity at 30 bar, where the NGZr catalyst presents higher selectivity for methanol than CZA and considerably lower selectivity for CO. Observing the CO/CH_3OH formation ratio, we can note the same trending in both reaction conditions. Decreasing the ratio of CO formation in relation to CH_3OH produced, as observed in NGZr compared to CZA catalyst, can favor the development of an industrial-viable process, considering recycle of unreacted gases, as CO can negatively impact the hydrogenation process in metal-based catalysts, due to sintering and competitive adsorption, affecting H_2 splitting [37].

3.2. Elucidating structural and chemical properties of oxide-supported Ni_5Ga_3 catalysts

The structural analysis by XRD of SiO_2, CeO_2, and ZrO_2 supports and Ni_5Ga_3 supported catalysts are presented in Fig. 2. For the NGSi catalyst, the main peaks referring to the crystalline Ni_5Ga_3 phase were identified, as well as their respective crystalline planes, and there was only a small decrease in peak intensity for SiO_2 support. For the NGZr and NGCe it was possible to identify only a small peak referring to the (221) crystalline plane of the Ni_5Ga_3 phase and a considerable decrease in the intensity of the peaks of ZrO_2 and CeO_2 supports. ZrO_2 support is well known to crystallize in different phases [25] and, in this case, monoclinic and tetragonal crystalline phases were identified and quantified by Rietveld refinement. Fig. 2B shows that our ZrO_2 support presents a predominance of the monoclinic phase with ~ 90%.

The Ni_5Ga_3 loading of the catalysts was assessed by ED-XRF analysis. The results in Table S3 show that the mass percentage of Ni + Ga reached values close to the expected amount of 17%. The Ni/Ga ratio was also calculated, in which all catalysts reached values close to the expected molar ratio for the 5Ni:3Ga ratio of 1.6. Transmission electron microscopy (TEM) images, particle size distribution, and elemental mapping of NGSi, NGCe, and NGZr catalysts after their reduction with H_2 are shown in Fig. S2. All the catalysts presented similar images, with very few differences between them. NGSi catalyst presented the broader particle size distribution, with the average particle size being around 14 nm. NGCe and NGZr, on the other hand, showed a narrow particle size distribution, in which the average particle size was around 11 and 10 nm, respectively. Elemental mapping showed a homogeneous metal distribution over the surface of catalysts, with no presence of spots containing isolated Ni and Ga phases, suggesting the formation of the

alloy phase, which is coherent with the presented XRD results.

The temperature-programmed reduction profiles for the catalysts are shown in Fig. 3A. All of them presented a major reduction peak in temperatures of 500, 600, and 700 °C for the catalysts NGCe, NGZr, and NGSi, respectively. Note that the NGCe and NGZr catalysts presented lower maximum reduction temperatures than the NGSi catalyst, which indicates that CeO_2 and ZrO_2 supports lead the alloy to reduce at lower temperatures than SiO_2. In addition to the main peak, the NGCe catalyst had two additional peaks around 250 °C and 800 °C. The first is probably generated due to the high mobility of alloy-support interfacial oxygen sites, which can be easily reduced at lower temperatures [38], while the last peak around 800 °C is generated by the reduction of Ce^{+4} to Ce^{+3} in the support surface [39]. The strong metal-support interaction (SMSI) effect is generally observed in reducible supports with metals of Group VIII [40–42], such as CeO_2. The presence of Ni-Ga alloy on the ceria surface lowered the Ce^{4+} to Ce^{3+} reduction temperature compared to bulk CeO_2 (Fig. S3). This behavior is commonly seen for transition metals, where the charge transfer effect from the nanoparticles to the support facilitates CeO_2 reduction. [43,44] Fig. 3A also shows the temperature-programmed reduction profiles of Ni and Ga supported on SiO_2, ZrO_2, and CeO_2 (dashed lines). These materials were prepared in the same way as the alloys, using the percentage of the Ni and Ga related to each metal percentage in the alloy (10.6% for Ni and 6.4% for Ga). Fig. S4 shows the TPR only for Ga-supported materials to better visualize its reduction peaks since its intensities are much lower than the other materials. The results show that the alloy reduces in different temperatures in relation to Ni-supported and Ga-supported in all cases, which evidences that the interactions of Ni and Ga in the alloy bring distinct properties compared to isolated metals. Table S6 shows the real and theoretical hydrogen consumption, and reduction degrees for the catalysts, supports, Ni-supported, and Ga-supported materials calculated from the TPR analysis. It can be noted from Table S6 that Ga-supported samples have a low reduction degree (21.3–34.4%), which means that it is hard to completely reduce Ga_2O_3 to Ga^0. An interesting behavior happens in the alloy, where apparently the gallium can be reduced much easier to form the alloy with nickel since the reduction degree of the alloy is 87% for NGSi and 100% for NGCe and NGZr catalysts.

The CO_2-TPD profiles of the catalysts are shown in Fig. 3B. CO_2 desorption peaks at lower temperatures (50–150 °C) were associated with weak basic sites. Desorption on moderate basic sites occurs between 150 and 300 °C and on stronger basic sites between 300 and 500 °C. Table 2 shows the quantification of curves for each region and the total amount of CO_2 desorbed on catalysts. NGSi presented the lowest amount of total basic sites (221.3 μmol g_{cat}^{-1}), followed by NGZr (233.6 μmol g_{cat}^{-1}) and NGCe (348.9 μmol g_{cat}^{-1}). A higher density of weak sites is present in NGSi (~ 44% of total basic sites) concerning the other catalysts (29% and 22% for NGZr and NGCe, respectively) evidencing the poor affinity of CO_2 with this catalyst. NGZr and NGCe presented most of CO_2 moderately/strongly adsorbed at the surface (71% and 78%, respectively) indicating considerable promoting effects in the interaction of CO_2 with catalyst surface generated by applying ZrO_2 and CeO_2 as supports in the Ni_5Ga_3 system. By correlating the number of moderate and strong basic sites with CO_2 conversion during hydrogenation reactions at different temperatures (Fig. S5), a linear growth of conversion can be noted by increasing the amount of these sites, which makes clear the relevance of modulating basicity to control the activity parameter during the reaction. Weak adsorption makes it harder for intramolecular bonds of CO_2 to be sufficiently stretched and weakened to allow intermediate stabilization, leading to low conversions, as observed for the NGSi catalyst. On the other hand, strong CO_2 adsorption and, consequently, strong intermediate adsorption, as expected by linear scaling relationships, can lead to an increase in the activation energy to further hydrogenate these species during reaction [45]. The accumulation of highly stable intermediates, *e.g.* CO, can lead to active site poisoning or facilitate its desorption as a product since high surface coverage tends to decrease the adsorption energy [46]. This

Table 1
Selectivity comparison for NGZr and $CuZnO/Al_2O_3$ (CZA) applied in the CO_2 hydrogenation at 270 °C and GHSV of and 8000 L kg_{cat}^{-1} h^{-1}.

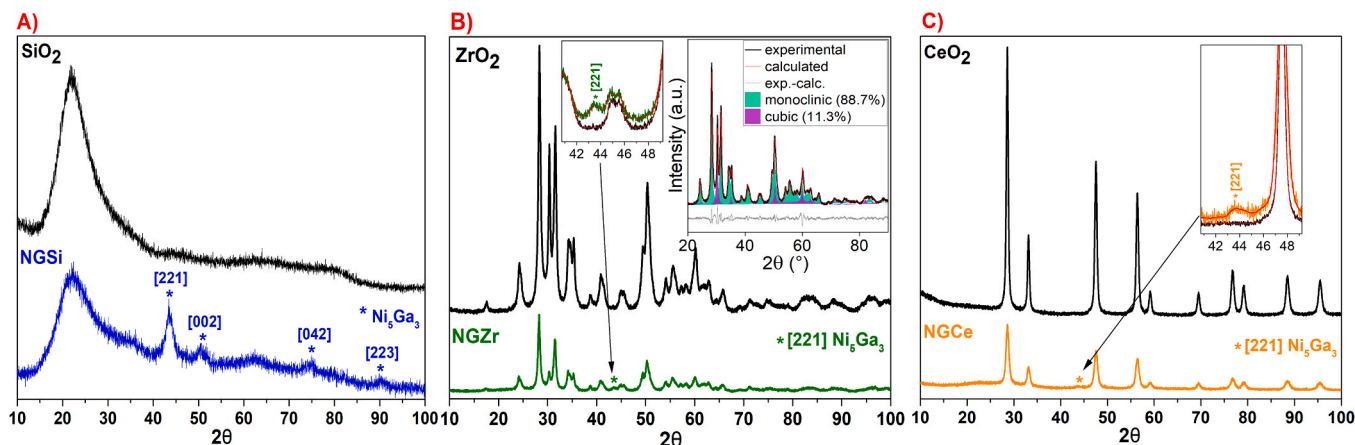| Catalyst	P (bar)	S_{CH3OH} (%)	S_{CO} (%)	CO/CH_3OH ratio
CZA	AP	0.07	99.14	1,416
NGZr	AP	0.81	95.74	118
CZA	30	23.44	76.24	3.25
NGZr	30	26.92	59.20	2.20

Fig. 2. XRD patterns of (A) NGSi catalyst and SiO_2 support; (B) NGZr catalyst and ZrO_2 support; (C) NGCe and CeO_2 support. The inset XRD pattern in (B) shows the Rietveld refinement of ZrO_2 support.
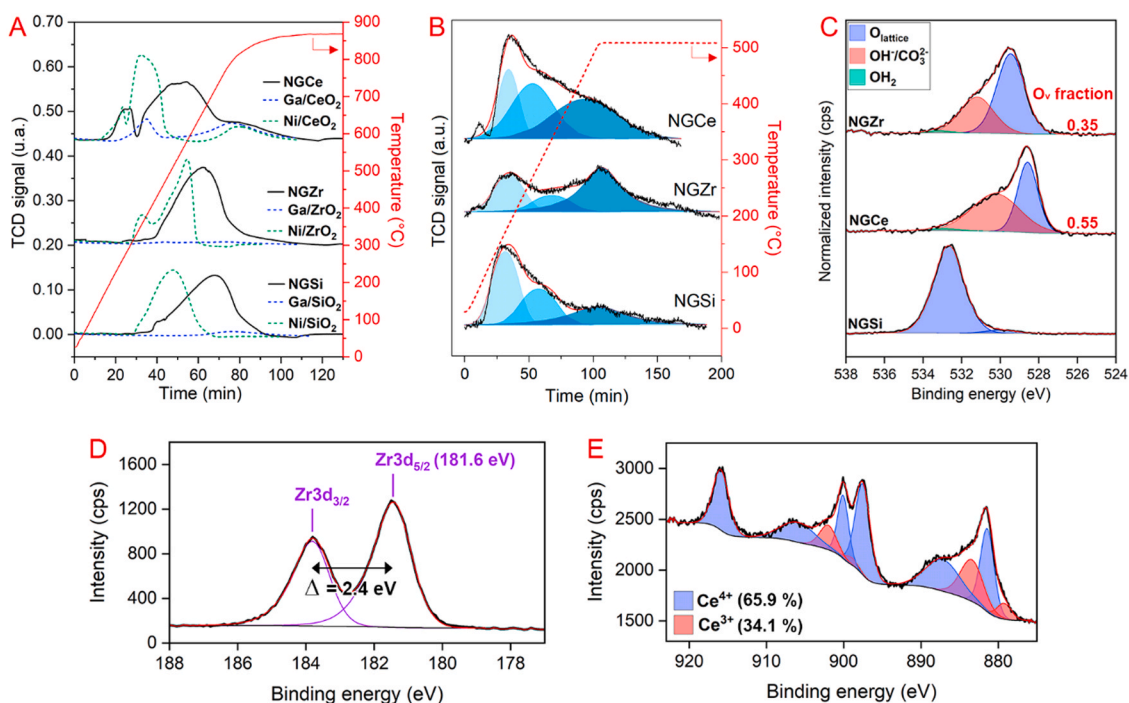

Fig. 3. (A) H_2-TPR and (B) CO_2-TPD profiles, and (C) O1s XPS spectra of NGSi, NGZr, and NGCe catalysts. (D) Zr 3d XPS spectra of NGZr catalyst and (E) Ce 3d XPS spectra of NGCe catalyst.

Table 2
Quantification of CO_2-TPD profiles for supported Ni-Ga catalysts.

Catalyst	Desorbed CO_2 ($\mu mol\ g_{cat.}^{-1}$)			
	Weakly bonded[a]	Moderately bonded[b]	Strongly bonded[c]	Total
NGSi	96.2	64.2	60.9	221.3
NGZr	67.8	37.6	128.2	233.6
NGCe	77.7	129.9	141.3	348.9

[a] Desorption peak with a maximum of around 150 °C (light blue area on Fig. 3B).

[b] Desorption peak with a maximum of around 300 °C (blue area on Fig. 3B).

[c] Desorption peak with a maximum of around 450 °C (dark blue area on Fig. 3B).

probably explains the higher CO selectivity in NGCe, even presenting a higher quantity of strong basic sites and, consequently, the higher conversion of CO_2 between catalysts.

The consumption of H_2 and the respective reduction degree, calculated by the ratio between experimental and nominal consumption, are shown in Table 3. These calculations were made using a TPR of the samples keeping the final temperature at 500 °C for 1 h, as it is made before the catalytic reaction. As the H_2-TPR profiles showed that the CeO_2 support is also reduced, the degree of reduction for alloy in this catalyst was determined by subtracting from the total value the hydrogen consumed relative to the reduction of the oxide surface. The reduction degree of the compound NGZr was the highest among all

Table 3

H$_2$ consumption and reduction degree of NGSi, NGZr, and NGCe calculated from the TPR of the catalysts keeping the final temperature at 500 °C for 1 h.

Sample	H$_2$ theoretical consumption (mmol g^{-1})[a]	H$_2$ real consumption (mmol g^{-1})	Reduction degree (%)
NGSi	2.77	1.72	62.1
NGZr	2.63	1.72	65.4
NGCe	2.75	1.11	40.4
CeO$_2$	–	0.52	–
ZrO$_2$	–	0.03	–

[a] Calculated from the amount of Ni and Ga impregnated according to ED-XRF results in Table S3.

catalysts, followed by NGSi and lastly NGCe. A higher reduction degree strongly suggests the formation of a greater number of exposed metal sites and, consequently, a superior capacity to dissociate and promote hydrogen spillover, which is a key step during hydrogenation reaction.

The high-resolution O1s XPS spectra of catalysts in Fig. 3C reveal the contribution of three distinct components, related to lattice oxygen (O$_{lattice}$), surface adsorbed water (OH$_2$), and the presence of hydroxyl and carbonate groups on the surface due to dissociative adsorption of H$_2$O and adsorption of CO$_2$ in structural defects generated by oxygen vacancies (OH$^-$/CO$_3^{2-}$) [47]. NGZr presents the O$_{lattice}$ component at ~ 529.6 eV, which corresponds to the binding energy of lattice oxygen of monoclinic ZrO$_2$. This observation is following Zr3d$_{5/2}$ binding energy (Fig. 3D) at 181.6 eV, with spin-orbit doublets d$_{5/2}$ and d$_{3/2}$ separated by 2.4 eV, characteristic of the monoclinic structure [48]. NGCe shows a component at ~ 528.6 eV related to lattice oxygen bonded to Ce in the CeO$_2$ structure [49]. The Ce3d spectrum (Fig. 3E) indicates the presence of around 34% of Ce^{3+} in NGCe catalyst. Due to high oxygen lability in the CeO$_2$ structure, is common to see the presence of Ce^{3+} species, which corroborates with the reduction peak related to CeO$_2$ support in the TPR profile. The O1s spectrum of NGSi showed a dominant peak at ~ 532.5 eV related to lattice oxygen of SiO$_2$ and a small peak at ~ 529.8 eV probably from lattice oxygen bonded to nickel and gallium in the interface with the support. The NGCe and NGZr spectra have a considerable contribution from the component at 531.4 eV indicating the presence of adsorbed oxygen, which is related to the presence of surface structural defects, like oxygen vacancies, while the NGSi catalyst has shown no peak related to these oxygen species. As suggested by TPR analysis (Table 3), XPS can confirm the formation of oxygen vacancies due to some reduction of the supports ZrO$_2$ and CeO$_2$, probably facilitated in the interface. It is known from the literature that oxygen vacancies can facilitate the adsorption and activation of CO$_2$ [24] and this behavior was observed through CO$_2$-TPD, which showed that NGCe and NGZr presented a higher amount of CO$_2$ adsorption compared to NGSi. The easier adsorption of CO$_2$ explains the higher conversion of these catalysts. The surface oxygen vacancy fraction (O$_v$ fraction in Fig. 3C) was estimated from the ratio between (OH$^-$/CO$_3^{2-}$) component of O1s XPS and the total amount of oxygen in the surface (O$_{lattice}$ + OH$^-$/CO$_3^{2-}$ + OH$_2$). The increase of 57% in the vacancy fraction, from 0.35 in NGZr to 0.55 in NGCe, is directly correlated to the increase in the number of moderately + strongly bonded CO$_2$, from TPD analysis from 165.8 μmol.g$_{cat}$$^{-1}$ in NGZr to 271.2 μmol g$_{cat}$$^{-1}$ in NGCe (increase of 63%), indicating that most of moderately and strongly bonded CO$_2$ are adsorbed on interface vacant sites.

Table 4

Surface properties of NGSi, NGZr, and NGCe catalysts.

Catalyst	S$_m$ (m$^2_{metal}$/g$_{cat}$)	Dispersion (%)	B.E.T. area (m^2 g$_{cat}$$^{-1}$)	Density of metallic sites (m$^2_{metal}$/m$^2_{support}$)
NGSi	51.5	40.0	80	0.33
NGZr	42.7	32.8	35	0.72
NGCe	27.1	21.9	73	0.42

The isotherms of N$_2$ adsorption/desorption (Fig. S6) for the catalysts and supports show that all samples presented isotherms of type II, according to the IUPAC classification [50], typical of non-porous materials. In Table 4, the values of specific surface area calculated by the BET method show that the material presenting the largest specific area is NGSi, followed by NGCe, and lastly NGZr. The low area of the NGZr catalyst is attributed to the predominant presence of the ZrO$_2$ monoclinic phase (Fig. 2B) already known in the literature for presenting the smallest area among all the ZrO$_2$ phases [25]. Table 4 also shows the values of the metallic area (S$_m$), the density of metallic sites, and dispersion, all calculated from the H$_2$-TPD analysis. The results indicate that the larger metallic area and dispersion are presented in NGSi catalyst, followed by NGZr and lastly NGCe. The representative survey XPS spectra of NGSi, NGCe, and NGZr catalysts (Fig. S7) show the main peaks related to Ni, Ga, Si, Ce, Zr, and O elements. It can be noted that the ratio between O1s related peak and the other peaks is much higher in the NGSi spectrum than NGCe and NGZr, which is related to the higher dispersion of the Ni-Ga on SiO$_2$, due to its high surface area compared to CeO$_2$ and ZrO$_2$, corroborating the results of dispersion calculated from H$_2$-TPD.

To better compare the presence of metallic sites between the catalysts, the density of metallic sites was determined by normalizing the metallic area by support surface area since BET area is quite different between the catalysts. NGZr has the highest surface coating by metallic sites, followed by NGCe and finally by NGSi. Although the high density of alloy covering catalyst surface, NGZr presented satisfactory dispersion, which indicates the formation of smaller metallic particles, which corroborate with TEM results. The superior productivity and TOF of the NGZr catalyst can be associated with these properties, which facilitate access to the active sites of the catalyst. The superior dispersion and metallic area of NGSi are probably the reason for its superior selectivity to methanol observed at lower temperatures, but this characteristic cannot explain alone the catalytic activity. Other intrinsic characteristics like CO$_2$ adsorption sites, previously seen in CO$_2$-TPD (Table 2), also contributes to the catalytic activity of the catalysts. The higher density of metallic sites together with the results observed in CO$_2$-TPD support the improved catalytic result of NGZr catalyst.
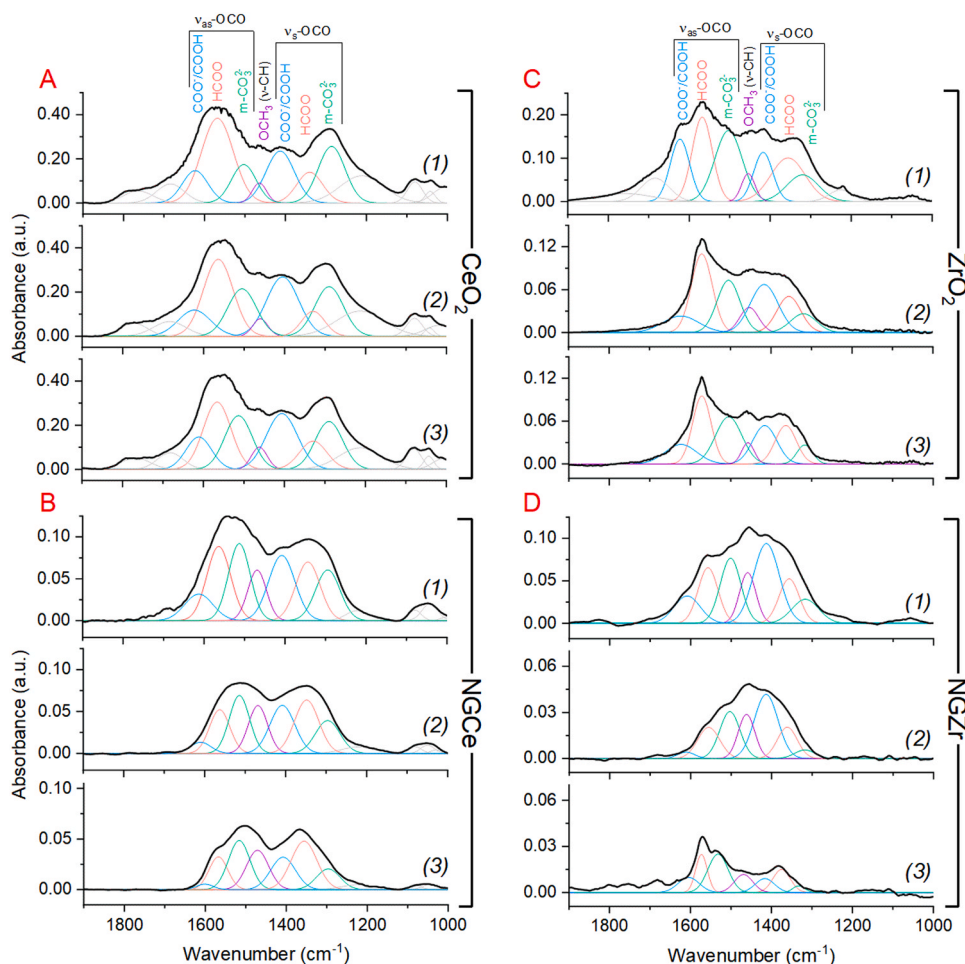
3.3. In situ DRIFTS study

By analyzing the physicochemical properties of the materials and the results in the hydrogenation of CO$_2$, it is clear that supports are playing an important role in determining activity and modulating the distribution of products for NGZr, NGCe, and NGSi catalysts. To gain insights into the role of the alloy-support interface in the stabilization of key reaction intermediates, *in situ* DRIFTS experiments were performed. When catalysts were exposed to CO$_2$/H$_2$ mixture at 270 °C (Fig. S8), four main regions are identified in the spectra: (1) C-O stretching of carbonate/carboxylate/formate adsorbed species in the region of 800–2000 cm^{-1} [51], (2) C-O stretching of carbon monoxide at 1800–2100 cm^{-1}, (3) gas-phase CO$_2$ at 2200–2500 cm^{-1}, and (4) C-H stretching of formate/methoxy species at 2700–3000 cm^{-1} [52]. It can be noted that for NGCe and NGZr surfaces, CO$_2$ is activated to form stable carbonate, carboxylate, and formate species, while in NGSi catalysts the formation of these species was not evidenced. These observations are in line with the CO$_2$-TPD profiles and XPS analysis, which showed a weak surface interaction of CO$_2$ and absence of defective oxygen sites in NGSi catalyst, and a moderate/strong interaction of CO$_2$, and the presence of a considerable amount of oxygen defective sites on the surface of NGZr and NGCe. Although no substantial adsorption and activation of CO$_2$ were evidenced in the NGSi surface, the catalyst still presented activity to methanol production with lower conversion. In our previous work [18], it was shown that unsupported Ni$_5$Ga$_3$ alloy mechanism passes by both formate and RWGS + CO-hydro routes, but with the gas-phase CO$_2$ direct binding dissociated hydrogen in the alloy surface, with no considerable formation of carbonate or carboxylate

intermediates that could be detected by infrared analysis. Probably, the same mechanism occurs on NGSi catalyst in this work, as indicated by the discrete formate bands at $\sim$ 1570 and $\sim$ 1360 cm^{-1} in the NGSi spectrum (Fig. S8). In this case, the support is acting only to favor the alloy dispersion when compared to the unsupported catalyst.
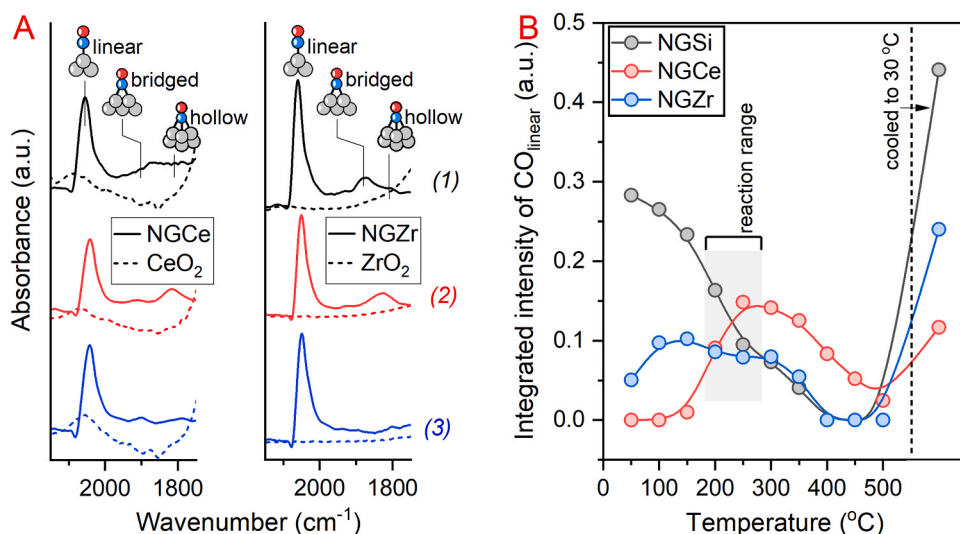
On the other hand, for NGZr and NGCe catalysts, the main differences in activity and methanol selectivity are probably arising from the stability and reactivity of surface species derived from CO$_2$ adsorption on the surface. To achieve a deep understanding of the role of carbonate, carboxylate, and formate in the process, these species were monitored by DRIFTS on the surface of the ZrO$_2$ and CeO$_2$ supports, and NGZr and NGCe catalysts, during separate steps of CO$_2$ adsorption (1), surface purge (2), and H$_2$ flow (3) as depicted in Fig. S9. The speciation of the steady-state spectrum of each step in Fig. 4 was made based on intervals of band position previously determined [51,53] for nanostructured ceria and zirconia materials. The most abundant species identified on the surface of materials are monodentate carbonates (m-CO$_3^{2-}$) with symmetric and asymmetric OCO stretchings at 1318 and 1502 cm^{-1}, formate (HCOO) with symmetric and asymmetric OCO stretchings at 1356 and 1568 cm^{-1}, carboxylate (COO$^-$/COOH) with symmetric and asymmetric OCO stretchings at 1416 and 1623 cm^{-1}, and methoxy (OCH$_3$) with CH stretching at 1456 cm^{-1}. The presence of hydrogenated species like *HCOO, *COOH, and small fractions of *OCH$_3$ in the CeO$_2$ and ZrO$_2$ supports (Fig. 4A and C), are probably due to the adsorption of CO$_2$ close to surface hydroxyl groups of oxides. After surface purge and H$_2$ flow, no considerable changes are seen, indicating low activity of

these intermediates to be hydrogenated in the supports solely. The catalytic reaction using the supports as catalysts was performed to support these observations. Table S4 shows the results, indicating an extremely low conversion ($<$ 0.2%) and no production of methanol on these supports.

By exposing NGCe and NGZr to CO$_2$ (Fig. 4B (1) and D (1)), an increase in the abundance of hydrogenated intermediates related to total adsorbed species was noted as compared to the supports, especially in the case of *OCH$_3$. This increase can be associated with the spillover of dissociated hydrogen available on the Ni-Ga surface from the previous reduction of the catalyst and with the interaction of the carbonates formed in the support-alloy interface. After purge and flow H$_2$ through the NGCe catalyst (Fig. 4B (2–3)), the profile of DRIFT spectra remained practically unchanged, indicating the high stability of these interfacial species and poor hydrogenation activity, which can explain the low methanol selectivity that NGCe catalyst presented. When the NGZr surface was exposed to H$_2$ flow (Fig. 4D (2–3)), a considerable decrease in abundance mainly related to carboxylate, formate, and methoxy intermediates are observed, indicating high hydrogenation activity of these species in NGZr catalyst. According to the reaction mechanism proposed by Kattel et al. [53], hydrogenation of carboxylate species is crucial and the initial step for both pathways (formate and rWGS + CO-hydro) to produce CH$_3$OH from CO$_2$. Additionally, hydrogenation of formate species (*HCOO) leading to further C—O bond cleavage and formation of *OCH$_3$ intermediate is essential to achieve CH$_3$OH *via* the formate pathway. Finally, the consumption of *OCH$_3$

Fig. 4. *In situ* DRIFT spectra in carbonate/formate region for (A) CeO$_2$, (B) NGCe, (C) ZrO$_2$ and (D) NGZr materials at 270 °C. The spectra were collected after 30 min exposure to a CO$_2$ flow (1), followed by a 30 min purge with N$_2$ (2) and, finally, 30 min of exposure to an H$_2$ flow (3). The materials were reduced *in situ* at 500 °C in an H$_2$ flow (30 mL min^{-1}) for 1 h before the experiments.

Fig. 5. (A) *In situ* DRIFT spectra in carbon monoxide region for CeO_2, NGCe, ZrO_2, and NGZr materials at 270 °C. The spectra were collected after 30 min exposure to a CO_2 flow (1), followed by a 30 min purge with N_2 (2) and, finally, 30 min of exposure to an H_2 flow (3). (B) The integrated intensities of linear CO species adsorbed in the H_2-preadsorbed surface of the catalysts at different temperatures. The materials were reduced *in situ* at 500 °C in an H_2 flow (30 mL min^{-1}) for 1 h before the experiments.

species indicates final hydrogenation and desorption as methanol.

The role of surface adsorbed CO was also investigated using the steps of CO_2 adsorption (1), surface purge (2), and H_2 flow (3), and the results are depicted in Fig. 5. Due to low activity, no considerable amounts of adsorbed CO were identified on the surface of pure CeO_2 and ZrO_2. Initially, three main bands related to CO linearly adsorbed, bridged, and 3-fold on hollow sites [54] are observed in the spectra for both NGZr and NGCe catalysts. After purge band related to 3-fold CO remains, and a decrease in linear CO and disappearance of bands related to bridged CO are noted, indicating that these species are desorbing as CO, or rearranging to other configurations since the surface covered by physisorbed CO is cleaned. By contacting the surface with an H_2 flow, the band related to linear CO remains unchanged, indicating a partial poisoning of the alloy surface by these species, and the 3-fold band disappears, suggesting the activity to evolve to further hydrogenated intermediates by rWGS + CO-hydro pathway in both catalysts. By these results, it can be suggested that rWGS + CO-hydro pathway is responsible for a small contribution to methanol production in these catalysts. Persistent CO species linearly adsorbed at the reaction temperature can directly affect the generation of dissociated hydrogen on the alloy surface by poisoning metallic sites, reducing the catalytic hydrogenation activity [55]. The integrated intensities of adsorbed linear CO in Fig. 5B, were obtained from DRIFT spectra collected by flowing CO in the H_2-preadsorbed surface of the catalysts at different temperatures (Fig. S10). At low temperatures, no considerable CO adsorption was noted on NGCe surface, while NGZr and NGSi presented linear CO species adsorbed on the catalyst surface, which is probably replacing hydrogen in the H_2-saturated alloy surface sites. At the reaction range of temperatures (180–270 °C), CO species adsorbed on NGSi substantially decreased, probably by desorption due to the weak interaction with this catalyst surface. This behavior can help to explain the higher methanol selectivity in NGSi sample at 180 °C (Table S5), where these species are probably available to be further hydrogenated to methanol. The amount of linear CO on NGZr surface at the reaction range of temperatures remained constant, and NGCe presented the maximum adsorption of CO at around 270 °C. The behavior presented by NGCe and NGZr can help to explain why the CO selectivity didn't increase for these catalysts with the temperature increase in the catalytic reaction. The CO interaction with NGZr and NGCe surfaces seems to be stronger than for NGSi, what explains the differences between the catalysts in terms of CO selectivity. By increasing the temperature to 500 °C, to clean the alloy surface, followed by decreasing to 30 °C under CO flow, it was noted that the adsorption of CO in the clean alloy surface of NGSi and NGZr, were considerable higher than the maximum adsorption observed in the

H_2-saturated surfaces, indicating that, even CO and H_2 presenting competitive adsorption, in the reaction temperatures a considerable amount of metallic sites are available for hydrogen activation. In the case of NGCe, the maximum capacity of CO adsorption in the clean surface is very close to the maximum CO adsorption in the H_2-saturated surface, which occurs in the reaction temperatures, indicating that these species are effectively poisoning the alloy surface sites in this catalyst. These results confirmed our previous discussion in CO_2-TPD data, which considered the linear scaling relationship for strong adsorption of reactants and intermediates, where high CO coverage are probably blocking hydrogenation activity and favoring the desorption of this intermediate as a product on NGCe.

Analyzing catalytic performance and *in situ* DRIFTS results, we conclude that both NGCe and NGZr can hydrogenate 3-fold CO adsorbed on hollow sites to form CH_3OH *via* rWGS + CO-hydro pathway, but the limited yield of CH_3OH evidenced in NGCe catalyst is more related to the initial steps of reaction where strong adsorption and, consequently, high stability of carboxylate, formate and CO intermediates seems to be poisoning active sites. On the other hand, the synergy in the interface formed by ZrO_2 and Ni-Ga alloy in NGZr seems to be strong enough to activate CO_2 but preventing active site poisoning, making this catalyst more effective to promote hydrogenation of $*CO_2^-$ for both: (1) formation $*CO$ and $*H_2O$ *via* rWGS pathway and (2) formation of $*HCOO$ and its further reduction to $*H_3CO$ and $*OH$ *via* formate pathway.

3.4. Theoretical results

The experimental results, in particular the *in situ* DRIFTS data, pointed to the existence of two distinct behaviors for the supported Ni_5Ga_3 catalyst: i) the first one is related to the role of interface for NGZr and NGCe catalysts, and ii) the second one that was observed for NGSi catalysts, which is similar to the behavior for unsupported Ni_5Ga_3 catalyst [18]. Thus, those findings indicate that the study of Ni_5Ga_3 unsupported and supported on ZrO_2 should be enough to tackle both experimentally observed behaviors. Thus, to further test the hypothesis raised by the experimental data, DFT calculations were performed to analyze the adsorption properties of CO_2, COOH, HCOO, H_2, and CO on clusters of Ni_5Ga_3, ZrO_2, and NGZr.

For the adsorbed structures, two energetic parameters were evaluated, the adsorption energy, E_{ad}, and the interaction energy, E_{int}. For a given system in which A is adsorbed on a system B, the three quantities are defined as:

$$E_{ad}^{A/B} = E_{tot}^{A/B} - E_{tot}^{A} - E_{tot}^{B} \qquad (9)$$

$$E_{int}^{A/B} = E_{tot}^{A/B} - E_{tot}^{A,fr} - E_{tot}^{B,fr} \qquad (10)$$

where E_{tot}^{A} is the total energy of the system with species A adsorbed on system B, E_{tot}^{A} and E_{tot}^{B} is the total energy for systems A and B relaxed, respectively. $E_{tot}^{A,fr}$ also $E_{tot}^{B,fr}$ are the single point energies for species A and B with their structures frozen as they are in the A/B system. The molecules' structural properties were also monitored for all the studied structures. Here, the largest molecule bond, d_{max}, is also shown for each adsorbate interacting with the Ni_5Ga_3, ZrO_2, and NGZr systems. Fig. 6 shows the lowest energy configurations for the adsorbates on each system accompanied by their adsorption and interaction energies, and largest molecule bond, while Fig. 7 shows the same properties for all calculated configurations.

The adsorption of CO_2 was experimentally observed only for NGZr and NGCe and not on unsupported Ni_5Ga_3. As shown in Fig. 7, the DFT calculations showed that CO_2 is better activated, with longer C—O bonds and stronger interaction energies, on both NGZr and $(ZrO_2)_{16}$ clusters. The adsorption energy on zirconia sites upon the formation of carbonate-like species, as shown in Fig. 6, was 4.23 eV lower than on the unsupported Ni_5Ga_3 and 4.42 eV lower than on the interface. Despite the stronger interaction energies felt by CO_2 at the NGZr interface as compared with the unsupported clusters, the adsorption energies for both cases are similar. This effect happens due to the higher CO_2 deformations induced by the adsorption at the interface, which competes with the interaction energies in the system stabilization [56,57]. The performed calculations also showed activation of CO_2 on unsupported Ni_5Ga_3 clusters which do not agree with experimental observations. This inconsistency can be attributed to the size differences between the considered theoretical model and experimental nanoparticles. It has been shown in recent works that a decrease in the size of transition-metal clusters can favor the CO_2 chemisorption and activation [58].

As discussed in the previous section, as opposed to Ni_5Ga_3 and NGZr, when the experiments are performed on isolated ZrO_2 supports, the changes on the identified adsorbed species upon H_2 flow are negligible. These results indicate that isolated ZrO_2 supports should not be efficient

for H_2 activation. Fig. 7 shows that the theoretical results agree with that statement. The adsorption energies for H_2 are about 0.4 eV stronger and the H—H bond lengths are about 0.15 A longer for supported and unsupported Ni_5Ga_3 than for the $(ZrO_2)_{16}$ clusters. Additionally, several structures of H_2 on $(ZrO_2)_{16}$ have adsorption energies very close to 0.0 eV and almost no H-H bond lengths elongation, which indicates the low interaction between both systems.

Additionally, for the CO_2 reduction experiments on ZrO_2 catalysts, no reaction was observed towards methanol; however, important intermediates for the reaction, such as carbonate and carboxylate, are observed on the catalyst surface. This behavior could be explained by the high stability of those species on the oxide. From the theoretical results, the adsorption of CO_2 on $(ZrO_2)_{16}$ preferentially occurs involving one O of the oxide to form carbonate species (Fig. 6), which agrees with experiments. The carbonate formation increases the stability of the whole system by more than 4 eV comparing with Ni_5Ga_3 and NGZr. Also, the *COOH and *HCOO are too stable on $(ZrO_2)_{16}$ surfaces, which is illustrated in Fig. 7. For these adsorbates, the adsorption energies were nearly 3 eV stronger on $(ZrO_2)_{16}$ than on Ni5Ga3 and NGZr, with no significant change in C-O bond lengths between the different substrates that could indicate much more activated species associated with such strong adsorption.

The comparison between the experimental data for ZrO_2 and NGZr systems also indicated that the *HCOO presence increased for NGZr systems as compared to the isolated support. This behavior can also be explained by the lack of H_2 activation on isolated ZrO_2 to hydrogenate CO_2. At the same time, the DFT calculations show that the difference in adsorption and interaction energies for $(ZrO_2)_{16}$ or NGZr are more significant for *HCOO than for *COOH. More specifically, *HCOO and *COOH adsorption energies are comparable on $(ZrO_2)_{16}$, while for NGZr the adsorption energy of *HCOO is 0.24 eV stronger than *COOH, which could help to explain the increase of formate species for the supported Ni_5Ga_3 as compared to ZrO_2 catalysts.

The experimental data also pointed to an absence of adsorbed CO on ZrO_2 catalysts, opposed to NGZr systems. As discussed before, this difference could be related to the low activity of the ZrO_2 catalysts to reduce CO_2, preventing the system to reduce intermediates to such species. Another contributing factor observed by DFT calculations is that the ZrO_2 system also shows negligible CO adsorption energies, especially when compared to Ni_5Ga_3 and NGZr systems, as observed in Fig. 7. This result also helps to explain the high CO selectivity observed for ZrO_2 system. Thus, despite the low activity of ZrO2 system to generate *CO, once this adsorbed is formed, the calculations show that it should easily desorb as a product. The calculations also showed that the interface strengthens the CO adsorption energies by 0.06 eV in comparison with isolated Ni_5Ga_3. This result could be related to the selectivity improvement towards methanol on the system since the stronger adsorption could favor further hydrogenation rather than CO desorption; however, further studies on the topic are necessary to understand the impact of this change in the reaction kinetics. Finally, the calculations also agree with the experiments in terms of CO adsorption site hierarchy, with the adsorption being favored on top sites. However, due to the cluster size, only top and bridge sites were observed, with the adsorption energy of CO on top sites being about 0.4 eV stronger than for bridge sites.

4. Insights into reaction mechanism over the Ni_5Ga_3/ZrO_2 catalyst

Combining the theoretical and experimental results, we propose a mechanism in Scheme 1 for the NGZr catalyst in the CO_2 hydrogenation. Methanol production on the catalyst surface follows two parallel pathways. The first one occurs in the alloy surface, where gas-phase CO_2 direct binds dissociated hydrogen to generate formate species that are further hydrogenated. The second one follows the adsorbed CO_2 on the alloy-support interface that is hydrogenated by the spillover of dissociated hydrogen from alloy to interface to form *HCOO and *COOH
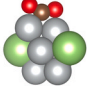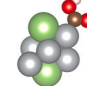

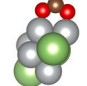**Fig. 6.** Lowest energy configuration for the adsorption of CO_2, H_2, COOH, HCOO, and CO on Ni_5Ga_3, $(ZrO_2)_{16}$ and NGZr, accompanied by their adsorption, E_{ad}, and the interaction energy, E_{int}, and the largest molecule bond d_{max}.
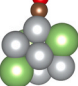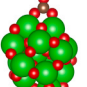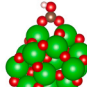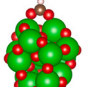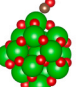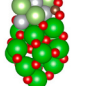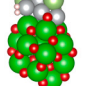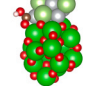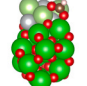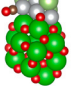
		CO_2	H_2	COOH	HCOO	CO
Ni_5Ga_3	E_{ad}	-1.19	-0.90	-2.65	-4.30	-2.24
	E_{int}	-2.79	-9.65	-2.86	-4.69	-2.37
	d_{max}	1.25	0.87	1.23	1.27	1.16
$(ZrO_2)_{16}$	E_{ad}	-5.70	-0.34	-7.00	-6.96	-0.85
	E_{int}	-6.18	-10.24	-7.53	-5.85	-0.87
	d_{max}	1.35	0.77	1.29	1.28	1.13
$Ni_5Ga_3/(ZrO_2)_{16}$	E_{ad}	-1.28	-0.84	-3.89	-4.13	-2.30
	E_{int}	-4.73	-9.43	-5.06	-4.82	-2.42
	d_{max}	1.29	0.89	1.28	1.28	1.16
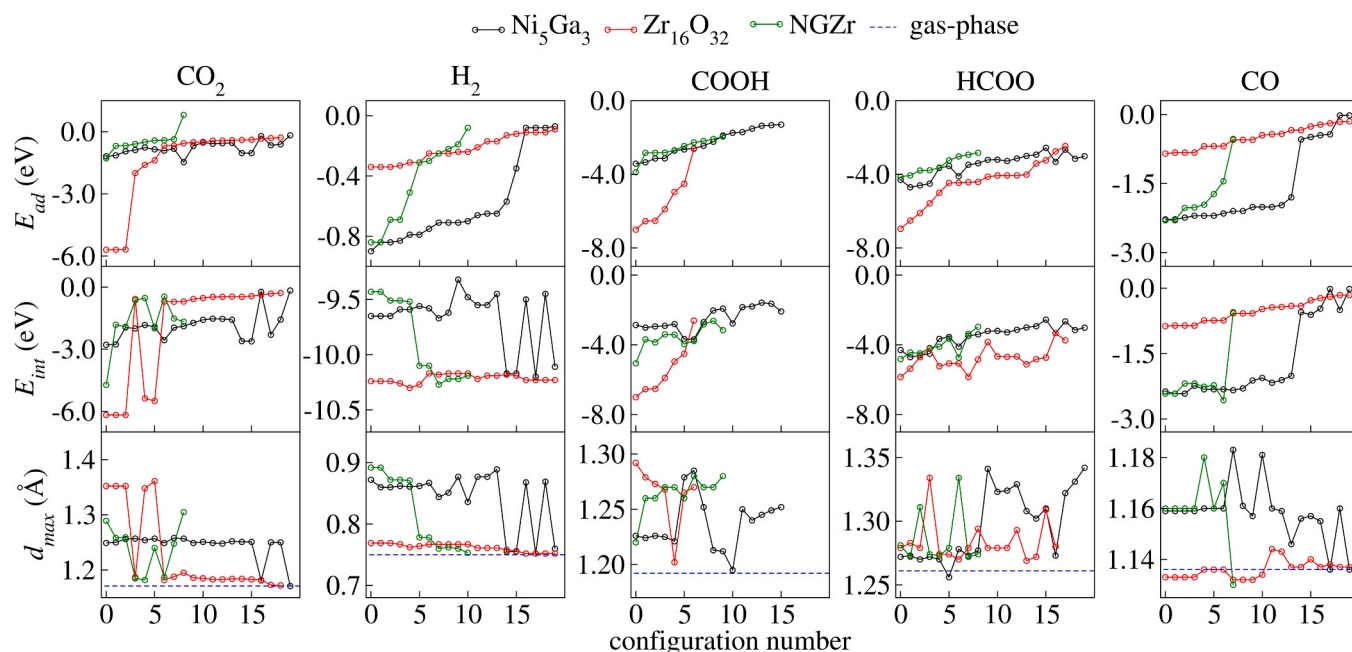
Fig. 7. Adsorption energy, E_{ad}, interaction energy, E_{int}, and largest molecule bond, d_{max}, for the obtained structures of CO_2 and H_2 adsorbed on Ni_5Ga_3, $(ZrO_2)_{16}$, and NGZr.
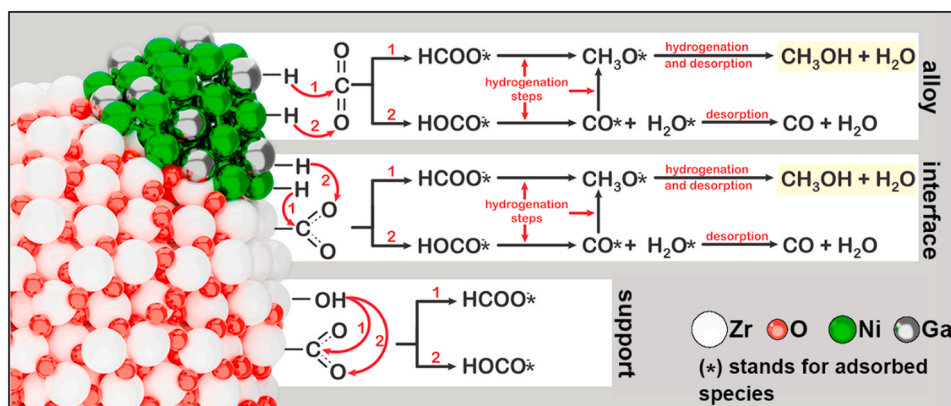
Scheme 1. Proposed mechanism for CO_2 hydrogenation of Ni_5Ga_3 supported on ZrO_2.

intermediates that are further hydrogenated to *OCH_3 by continuous H_2 dissociation and spillover resulting in methanol. For the first pathway, occurring on the alloy surface, there is no evidence of the influence of the support, and it should occur in the three systems studied in this work, as well as in the unsupported Ni_5Ga_3 alloy as observed in the previous studies [18]. The second pathway was not evidenced in NGSi and unsupported Ni_5Ga_3 alloy, being characteristic for NGZr and NGCe catalysts, that moderately/strongly bind CO_2. DRIFT spectra revealed that adsorbed CO_2 species are very stable in the NGCe interface, avoiding further hydrogenation in the presence of H_2, while in the NGZr these species are hydrogenated. Finally, in the ZrO_2 surface, adsorption of CO_2 is favored, and the presence of carboxylate and formate species is noted, probably associated with the interaction with hydroxyl groups of oxide. These species are highly stabilized in the ZrO_2 and the limitations in the H_2 dissociation and spillover in the oxide surface disfavor the hydrogenation to methanol. Therefore, methanol production by CO_2 hydrogenation on NGZr probably occurs by formate and rWGS + CO-hydro routes through parallel pathways by intermediates of adsorbed CO_2 in alloy-ZrO_2 interface and by CO_2 direct binding to dissociated hydrogen in the alloy surface, which justifies the increase in productivity.

5. Conclusions

SiO_2, ZrO_2, and CeO_2-supported Ni_5Ga_3 catalysts were prepared by a wet impregnation method and tested as candidates for CO_2 reduction to methanol. The XRD and ED-XRF analysis showed that the materials achieved the expected structural and compositional properties. TEM images and EDS mapping revealed a homogeneous distribution of Ni-Ga atoms over the surface, suggesting the alloy formation. From the three supported alloys, NGZr showed superior catalytic activity towards methanol. This behavior was attributed to the combination of moderate CO_2 adsorption strength and high density of exposed metallic sites of NGZr catalyst that help the intermediate stabilization and hydrogen spillover. As evidenced by *in situ* DRIFTS analysis, the strong adsorption of intermediates in the NGCe alloy-support interface poisoned potential active sites, avoiding further hydrogenation to methanol, while poor affinity to adsorb CO_2 in the NGSi interface limits the methanol production through the alloy surface route. NGZr presented high consumption of interfacial carboxylate, formate, and methoxy intermediates in the presence of hydrogen, indicating high hydrogenation activity of these species and, suggesting that methanol productivity follows two parallel pathways (rWGS and formate) by routes in different

surfaces (alloy and alloy-support interface), which explains the increase in the productivity. The adsorption energy, interaction energy, and bond lengths, calculated by DFT for reactants and intermediates in the surface of Ni_5Ga_3, $(ZrO_2)_{16}$, and $Ni_5Ga_3/(ZrO_2)_{16}$ systems, supported the experimental conclusions allowing to propose a reaction mechanism for the Ni_5Ga_3/ZrO_2 system. Overall, this study highlights the importance of alloy-support synergy, for supported Ni_5Ga_3 systems, to optimize methanol production from CO_2. Also, these findings can contribute to advance in the understanding of key mechanistic features of supported-Ni-Ga alloys in this reaction.

CRediT authorship contribution statement

Letícia F. Rasteiro: Prepared the materials and conducted catalytic tests, Designed and conducted the experiments, Contributed to the manuscript writing. **Luiz H. Vieira:** Designed and conducted the experiments, Contributed to the manuscript writing. **Rafael A. De Sousa:** Performed the DFT calculations, Contributed to the manuscript writing. **Vivianne K. Ocampo-Restrepo:** Performed the DFT calculations, Contributed to the manuscript writing. **Lucas G. Verga:** Performed the DFT calculations, Contributed to the manuscript writing. **Elisabete M. Assaf:** Supervised and coordinated the project. **Juarez L. F. Da Silva:** Supervised and coordinated the project. **José M. Assaf:** Supervised and coordinated the project. All authors discussed and revised the manuscript.

Declaration of Competing Interest

The authors declare no competing financial interest.

Acknowledgments

Appendix A. Supporting information

Supplementary data associated with this article can be found in the online version at doi:10.1016/j.apcatb.2021.120842.

References

[1] A. Álvarez, A. Bansode, A. Urakawa, A.V. Bavykina, T.A. Wezendonk, M. Makkee, J. Gascon, F. Kapteijn, Challenges in the greener production of formates/formic acid, methanol, and DME by heterogeneously catalyzed CO_2 hydrogenation processes, Chem. Rev. 117 (14) (2017) 9804–9838, https://doi.org/10.1021/acs.chemrev.6b00816.

[2] T.A. Atsbha, T. Yoon, P. Seongho, C.J. Lee, A review on the catalytic conversion of CO_2 using H_2 for synthesis of CO, methanol, and hydrocarbons, J. CO2 Util. 44 (2021), 101413, https://doi.org/10.1016/j.jcou.2020.101413.

[3] W.C. Liu, J. Baek, G.A. Somorjai, The methanol economy: methane and carbon dioxide conversion, Top. Catal. 61 (7–8) (2018) 530–541, https://doi.org/10.1007/s11244-018-0907-4.

[4] Y. Men, X. Fang, Q. Gu, R. Singh, F. Wu, P. Danaci, Q. Zhao, P. Xiao, P.A. Webley, Synthesis of Ni_5Ga_3 catalyst by hydrotalcite-like compound (HTlc) precursors for CO_2 hydrogenation to methanol, Appl. Catal. B Environ. 275 (2020), 119067, https://doi.org/10.1016/j.apcatb.2020.119067.

[5] A.A. Olajire, Valorization of greenhouse carbon dioxide emissions into value-added products by catalytic processes, J. CO2 Util. 3–4 (2013) 74–92, https://doi.org/10.1016/j.jcou.2013.10.004.

[6] X. Jiang, X. Nie, X. Guo, C. Song, J.G. Chen, Recent advances in carbon dioxide hydrogenation to methanol via heterogeneous catalysis, Chem. Rev. 120 (15) (2020) 7984–8034, https://doi.org/10.1021/acs.chemrev.9b00723.

[7] I.U. Din, M.S. Shaharun, M.A. Alotaibi, A.I. Alharthi, A. Naeem, Recent developments on heterogeneous catalytic CO_2 reduction to methanol, J. CO2 Util. 34 (2019) 20–33, https://doi.org/10.1016/j.jcou.2019.05.036.

[8] D. Bellotti, M. Rivarolo, L. Magistri, A.F. Massardo, Feasibility study of methanol production plant from hydrogen and captured carbon dioxide, J. CO2 Util. 21 (2017) 132–138, https://doi.org/10.1016/j.jcou.2017.07.001.

[9] N. Rui, Z. Wang, K. Sun, J. Ye, Q. Ge, C. Jun Liu, CO_2 hydrogenation to methanol over Pd/In_2O_3: effects of Pd and oxygen vacancy, Appl. Catal. B Environ. 218 (2017) 488–497, https://doi.org/10.1016/j.apcatb.2017.06.069.

[10] H. Jiang, J.; Lin, X. Wu, W. Wang, Y. Chen, M. Zhang, Efficient hydrogenation of CO_2 to methanol over $Pd/In_2O_3/SBA-15$ catalysts, J. CO2 Util. 36 (2020) 33–39, https://doi.org/10.1016/j.jcou.2019.10.013.

[11] E.S. Gutterød, A. Lazzarini, T. Fjermestad, G. Kaur, M. Manzoli, S. Bordiga, S. Svelle, K.P. Lillerud, E. Skúlason, S. Øien-ØDegaard, A. Nova, U. Olsbye, Hydrogenation of CO_2 to methanol by Pt nanoparticles encapsulated in UiO-67: deciphering the role of the metal-organic framework, J. Am. Chem. Soc. 142 (2) (2020) 999–1009, https://doi.org/10.1021/jacs.9b10873.

[12] B. Rungtaweevoranit, J. Baek, J.R. Araujo, B.S. Archanjo, K.M. Choi, O.M. Yaghi, G.A. Somorjai, Copper nanocrystals encapsulated in Zr-based metal-organic frameworks for highly selective CO_2 hydrogenation to methanol, Nano Lett. 16 (12) (2016) 7645–7649, https://doi.org/10.1021/acs.nanolett.6b03637.

[13] A. Pustovarenko, A. Dikhtiarenko, A. Bavykina, L. Gevers, A. Ramírez, A. Russkikh, S. Telalovic, A. Aguilar, J.L. Hazemann, S. Ould-Chikh, J. Gascon, Metal-organic framework-derived synthesis of cobalt indium catalysts for the hydrogenation of CO_2 to methanol, ACS Catal. 10 (9) (2020) 5064–5076, https://doi.org/10.1021/acscatal.0c00449.

[14] E.M. Fiordaliso, I. Sharafutdinov, H.W.P. Carvalho, J.D. Grunwaldt, T.W. Hansen, I. Chorkendorff, J.B. Wagner, C.D. Damsgaard, Intermetallic $GaPd_2$ nanoparticles on SiO_2 for low-pressure CO_2 hydrogenation to methanol: catalytic performance and in situ characterization, ACS Catal. 5 (10) (2015) 5827–5836, https://doi.org/10.1021/acscatal.5b01271.

[15] X. Jiang, N. Koizumi, X. Guo, C. Song, Bimetallic Pd – Cu catalysts for selective CO_2 hydrogenation to methanol, Appl. Catal. B Environ. 171 (2015) 173–185.

[16] F. Studt, I. Sharafutdinov, F. Abild-Pedersen, C.F. Elkjær, J.S. Hummelshøj, S. Dahl, I. Chorkendorff, J.K. Nørskov, Discovery of a Ni-Ga catalyst for carbon dioxide reduction to methanol, Nat. Chem. 6 (4) (2014) 320–324, https://doi.org/10.1038/nchem.1873.

[17] P. Chen, G. Zhao, Y. Liu, Y. Lu, Monolithic $Ni_5Ga_3/SiO_2/Al_2O_3/Al$-fiber catalyst for CO_2 hydrogenation to methanol at ambient pressure, Appl. Catal. A Gen. 562 (2018) 234–240, https://doi.org/10.1016/j.apcata.2018.06.021.

[18] L.F. Rasteiro, M.A.L.S. Rossi, J.M. Assaf, E.M. Assaf, Low-pressure hydrogenation of CO_2 to methanol over Ni-Ga alloys synthesized by a surfactant-assisted co-precipitation method and a proposed mechanism by DRIFTS analysis, Catal. Today (2020) 1–11, https://doi.org/10.1016/j.cattod.2020.05.067.

[19] I. Sharafutdinov, C. Fink, H. Wallace, P. Carvalho, De, D. Gardini, G. Luca, C. Danvad, J. Birkedal, J. Grunwaldt, S. Dahl, I. Chorkendorff, Intermetallic compounds of Ni and Ga as catalysts for the synthesis of methanol, J. Catal. 320 (2014) 77–88, https://doi.org/10.1016/j.jcat.2014.09.025.

[20] R. Goyal, W.J. Lee, S. Sameer, B. Sarkar, K. Chiang, A. Bordoloi, CN_x stabilized Ni-Ga nanoparticles for CO_2 hydrogenation: role of preparation methods, Catal. Today (2019), https://doi.org/10.1016/j.cattod.2019.03.031.

[21] T.E.L. Smitshuysen, M.R. Nielsen, T. Pruessmann, A. Zimina, T.L. Sheppard, J. D. Grunwaldt, I. Chorkendorff, C.D. Damsgaard, Optimizing Ni−Fe−Ga Alloys into Ni_2FeGa for the hydrogenation of CO_2 into methanol, ChemCatChem 12 (12) (2020) 3265–3273, https://doi.org/10.1002/cctc.202000174.

[22] A. Gallo, J.L. Snider, D. Sokaras, D. Nordlund, T. Kroll, H. Ogasawara, L. Kovarik, M.S. Duyar, T.F. Jaramillo, Ni_5Ga_3 catalysts for CO_2 reduction to methanol: exploring the role of Ga surface oxidation/reduction on catalytic activity, Appl. Catal. B Environ. 267 (2020), 118369, https://doi.org/10.1016/J.APCATB.2019.118369.

[23] M.S. Duyar, A. Gallo, J.L. Snider, T.F. Jaramillo, Low-pressure methanol synthesis from CO_2 over metal-promoted Ni-Ga intermetallic, Catal. J. CO2 Util. 39 (2020), 101151, https://doi.org/10.1016/j.jcou.2020.03.001.

[24] W. Wang, Z. Qu, L. Song, Q. Fu, CO_2 hydrogenation to methanol over Cu/CeO_2 and Cu/ZrO_2 catalysts: tuning methanol selectivity via metal-support interaction, J. Energy Chem. (2019) https://doi.org/.1037//0033-2909.I26.1.78.

[25] T. Witoon, J. Chalorngtham, P. Dumrongbunditkul, M. Chareonpanich, J. Limtrakul, CO_2 hydrogenation to methanol over Cu/ZrO_2 catalysts: effects of zirconia phases, Chem. Eng. J. 293 (2016) 327–336, https://doi.org/10.1016/j.cej.2016.02.069.

[26] B. Ouyang, W. Tan, B. Liu, Morphology effect of nanostructure ceria on the Cu/CeO_2 catalysts for synthesis of methanol from CO_2 hydrogenation, Catal. Commun. 95 (2017) 36–39, https://doi.org/10.1016/j.catcom.2017.03.005.

[27] E. Lam, K. Larmier, P. Wolf, S. Tada, O.V. Safonova, C. Copéret, Isolated Zr surface sites on silica promote hydrogenation of CO_2 to CH_3OH in supported Cu catalysts, J. Am. Chem. Soc. 140 (33) (2018) 10530–10535, https://doi.org/10.1021/jacs.8b05595.

[28] I. Ud Din, M.S. Shaharun, D. Subbarao, A. Naeem, Synthesis, characterization and activity pattern of carbon nanofibers based copper/zirconia catalysts for carbon dioxide hydrogenation to methanol: influence of calcination temperature, J. Power Sources 274 (2015) 619–628, https://doi.org/10.1016/j.jpowsour.2014.10.087.

[29] J.P. Perdew, K. Burke, M. Ernzerhof, Generalized gradient approximation made simple, Phys. Rev. Lett. 77 (18) (1996) 3865–3868, https://doi.org/10.1103/PhysRevLett.77.3865.

[30] A. Tkatchenko, M. Scheffler, Accurate molecular van Der Waals interactions from ground-state electron density and free-atom reference data, Phys. Rev. Lett. 102 (7) (2009), 073005, https://doi.org/10.1103/PhysRevLett.102.073005.

[31] V. Blum, R. Gehrke, F. Hanke, P. Havu, V. Havu, X. Ren, K. Reuter, M. Scheffler, Ab initio molecular simulations with numeric atom-centered orbitals, Comput. Phys. Commun. 180 (11) (2009) 2175–2196, https://doi.org/10.1016/j.cpc.2009.06.022.

[32] A.R. Puigdollers, F. Illas, G. Pacchioni, Structure and properties of zirconia nanoparticles from density functional theory calculations, J. Phys. Chem. C 120 (8) (2016) 4392–4402, https://doi.org/10.1021/acs.jpcc.5b12185.

[33] S.P. Lloyd, Least squares quantization in PCM, IEEE Trans. Inf. Theory 28 (2) (1982) 129–137, https://doi.org/10.1109/TIT.1982.1056489.

[34] S.-H. Cha, Comprehensive survey on distance/similarity measures between probability density functions, Int. J. Math. Model. Methods Appl. Sci. 1 (4) (2007) 300–307.

[35] R. Gehrke, K. Reuter, Assessing the efficiency of first-principles basin-hopping sampling, Phys. Rev. B - Condens. Matter Mater. 79 (8) (2009), 085412, https://doi.org/10.1103/PhysRevB.79.085412.

[36] M. Boudart, Turnover rates in heterogeneous catalysis, Chem. Rev. 95 (3) (1995) 661–666, https://doi.org/10.1021/cr00035a009.

[37] T.P. Araújo, A. Shah, C. Mondelli, J.A. Stewart, D. Curulla Ferré, J. Pérez-Ramírez, Impact of hybrid CO_2-CO feeds on methanol synthesis over In_2O_3-based catalysts, Appl. Catal. B Environ. 285 (2021), 119878, https://doi.org/10.1016/J.APCATB.2021.119878.

[38] S. Mahammadunnisa, P. Manoj Kumar Reddy, N. Lingaiah, C. Subrahmanyam, $NiO/Ce_{1-x}Ni_xO_{2-\delta}$ as an alternative to noble metal catalysts for CO oxidation, Catal. Sci. Technol. 3 (3) (2013) 730–736, https://doi.org/10.1039/c2cy20641b.

[39] I.Y. Habib, J. Burhan, F. Jaladi, C.M. Lim, A. Usman, N.T.R.N. Kumara, S.C. E. Tsang, A.H. Mahadi, Effect of Cr doping in CeO_2 nanostructures on photocatalysis and H_2O_2 assisted methylene blue dye degradation, Catal. Today 2019 (2020) 1–8, https://doi.org/10.1016/j.cattod.2020.04.008.

[40] S.J. Tauster, Strong metal-support interactions, Acc. Chem. Res. 20 (11) (1987) 389–394.

[41] C.J. Pan, M.C. Tsai, W.N. Su, J. Rick, N.G. Akalework, A.K. Agegnehu, S.Y. Cheng, B.J. Hwang, Tuning/exploiting strong metal-support interaction (SMSI) in heterogeneous catalysis, J. Taiwan Inst. Chem. Eng. 74 (2017) 154–186, https://doi.org/10.1016/j.jtice.2017.02.012.

[42] S.J. Tauster, S.C. Fung, R.T.K. Baker, J.A. Horsley, Strong interactions in catalysts, Science 211 (4487) (1981) 1121–1125 (80-).

[43] P. Tereshchuk, R.L.H. Freire, C.G. Ungureanu, Y. Seminovski, A. Kiejna, J.L.F. Da Silva, The role of charge transfer in the oxidation state change of Ce atoms in the TM_{13}-CeO_2(111) systems (TM = Pd, Ag, Pt, Au): a DFT + U investigation, Phys. Chem. Chem. Phys. 17 (20) (2015) 13520–13530, https://doi.org/10.1039/c4cp06016d.

[44] A.S. Thill, A.S. Kilian, F. Bernardi, Key role played by metallic nanoparticles on the ceria reduction, J. Phys. Chem. C 121 (45) (2017) 25323–25332, https://doi.org/10.1021/acs.jpcc.7b09013.

[45] A.O. Elnabawy, J. Schumann, P. Bothra, A. Cao, J.K. Nørskov, The challenge of CO hydrogenation to methanol: fundamental limitations imposed by linear scaling relations, Top. Catal. 63 (7–8) (2020) 635–648, https://doi.org/10.1007/s11244-020-01283-2.

[46] T.C. Bromfield, D.C. Ferré, J.W. Niemantsverdriet, A DFT study of the adsorption and dissociation of CO on Fe(100): influence of surface coverage on the nature of accessible adsorption states, ChemPhysChem 6 (2) (2005) 254–260, https://doi.org/10.1002/cphc.200400452.

[47] L.B. Lopes, L.H. Vieira, J.M. Assaf, E.M. Assaf, Effect of Mg substitution on $LaTi_{1-x}Mg_xO_{3+\delta}$ catalysts for improving the C_2 selectivity of the oxidative coupling of methane, Catal. Sci. Technol. 11 (1) (2021) 283–296, https://doi.org/10.1039/d0cy01783c.

[48] P. Lackner, Z. Zou, S. Mayr, U. Diebold, M. Schmid, Using photoelectron spectroscopy to observe oxygen spillover to zirconia, Phys. Chem. Chem. Phys. 21 (32) (2019) 17613–17620, https://doi.org/10.1039/c9cp03322j.

[49] S. Soni, V.S. Vats, S. Kumar, B. Dalela, M. Mishra, R.S. Meena, G. Gupta, P.A. Alvi, S. Dalela, Structural, optical and magnetic properties of Fe-doped CeO_2 samples probed using X-Ray photoelectron spectroscopy, J. Mater. Sci. Mater. Electron. 29 (12) (2018) 10141–10153, https://doi.org/10.1007/s10854-018-9060-x.

[50] M.D. Donohue, G.L. Aranovich, Classification of Gibbs adsorption isotherms, Adv. Colloid Interface Sci. 76–77 (1998) 137–152, https://doi.org/10.1016/S0001-8686(98)00044-X.

[51] M. Piumetti, S. Bensaid, D. Fino, N. Russo, Nanostructured ceria-zirconia catalysts for CO oxidation: study on surface properties and reactivity, Appl. Catal. B Environ. 197 (2016) 35–46, https://doi.org/10.1016/j.apcatb.2016.02.023.

[52] C. Wu, L. Lin, J. Liu, J. Zhang, F. Zhang, T. Zhou, N. Rui, S. Yao, Y. Deng, F. Yang, W. Xu, J. Luo, Y. Zhao, B. Yan, X.D. Wen, J.A. Rodriguez, D. Ma, Inverse ZrO_2/Cu as a highly efficient methanol synthesis catalyst from CO_2 hydrogenation, Nat. Commun. 11 (1) (2020) 1–10, https://doi.org/10.1038/s41467-020-19634-8.

[53] S. Kattel, B. Yan, Y. Yang, J.G. Chen, P. Liu, Optimizing binding energies of key intermediates for CO_2 hydrogenation to methanol over oxide-supported copper, J. Am. Chem. Soc. 138 (38) (2016) 12440–12450, https://doi.org/10.1021/jacs.6b05791.

[54] T.S. Galhardo, A.H. Braga, B.H. Arpini, J. Szanyi, R.V. Gonçalves, B.F. Zornio, C. R. Miranda, L.M. Rossi, Optimizing active sites for high CO selectivity during CO_2 hydrogenation over supported nickel catalysts, J. Am. Chem. Soc. 143 (2021), https://doi.org/10.1021/jacs.0c12689 (4280-4280).

[55] S. Xu, S. Chansai, S. Xu, C.E. Stere, Y. Jiao, S. Yang, C. Hardacre, X. Fan, CO poisoning of Ru catalysts in CO_2 hydrogenation under thermal and plasma conditions: a combined kinetic and diffuse reflectance infrared fourier transform spectroscopy-mass spectrometry study, ACS Catal. 10 (21) (2020) 12828–12840, https://doi.org/10.1021/acscatal.0c03620.

[56] V.K. Ocampo-Restrepo, L. Zibordi-Besse, J.L.F. Da Silva, Ab initio investigation of the atomistic descriptors in the activation of small molecules on 3d transition-metal 13-atom clusters: the example of H_2, CO, H_2O, and CO_2, J. Chem. Phys. 151 (21) (2019), 214301, https://doi.org/10.1063/1.5125769.

[57] P.C.D. Mendes, L.G. Verga, J.L.F. Da Silva, Ab initio screening of Pt-based transition-metal nanoalloys using descriptors derived from the adsorption and activation of CO_2, Phys. Chem. Chem. Phys. 23 (10) (2021) 6029–6041, https://doi.org/10.1039/d1cp00570g.

[58] P.C.D. Mendes, V.K. Ocampo-Restrepo, J.L.F. Da Silva, Ab initio investigation of quantum size effects on the adsorption of CO_2, CO, H_2O, and H_2 on transition-metal particles, Phys. Chem. Chem. Phys. 22 (16) (2020) 8998–9008, https://doi.org/10.1039/d0cp00880j.